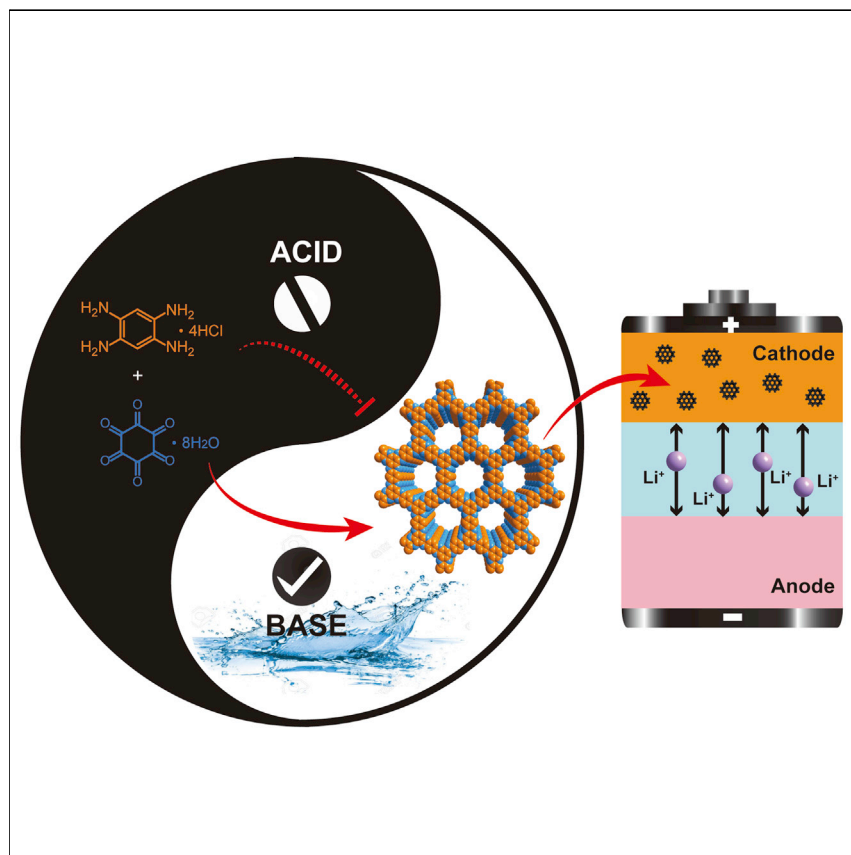


## Article

# Dynamic Covalent Synthesis of Crystalline Porous Graphitic Frameworks



We report the unusual dynamic characteristics of the C=N bonds in the pyrazine ring promoted under basic aqueous conditions, which enables the successful synthesis of two-dimensional porous graphitic frameworks (PGFs) featuring fully annulated aromatic skeletons and periodic pores. The PGF displayed high electrical conductivity and remarkable performance as a cathode material for lithium-ion batteries, far outperforming the amorphous counterparts in terms of capacity and cycle stability.

Xinle Li, Hongxia Wang, Hao Chen, ..., Emory M. Chan, Jian Zhang, Yi Liu

jianzhang@lbl.gov (J.Z.)  
yliu@lbl.gov (Y.L.)

## HIGHLIGHTS

The dynamic characteristics of C=N bonds in aromatic pyrazine rings has been reported

The dynamics enabled the synthesis of a crystalline porous 2D graphitic framework

The periodic feature was directly visualized using transmission electron microscopy

The framework displays outstanding performance as a cathode for lithium-ion batteries



## Article

# Dynamic Covalent Synthesis of Crystalline Porous Graphitic Frameworks

Xinle Li,<sup>1,11</sup> Hongxia Wang,<sup>4,11</sup> Hao Chen,<sup>4,11</sup> Qi Zheng,<sup>2,11</sup> Qiubo Zhang,<sup>2</sup> Haiyan Mao,<sup>3,5,10</sup> Yawei Liu,<sup>1</sup> Songliang Cai,<sup>1,7</sup> Bing Sun,<sup>1,8</sup> Chaochao Dun,<sup>1</sup> Madeleine P. Gordon,<sup>1</sup> Haimei Zheng,<sup>2,6</sup> Jeffrey A. Reimer,<sup>3,5</sup> Jeffrey J. Urban,<sup>1</sup> Jim Ciston,<sup>1</sup> Tianwei Tan,<sup>9</sup> Emory M. Chan,<sup>1</sup> Jian Zhang,<sup>1,\*</sup> and Yi Liu<sup>1,12,\*</sup>

## SUMMARY

Porous graphitic framework (PGF) is a two-dimensional (2D) material that has emerging energy applications. An archetype contains stacked 2D layers, the structure of which features a fully annulated aromatic skeleton with embedded heteroatoms and periodic pores. Due to the lack of a rational approach in establishing in-plane order under mild synthetic conditions, the structural integrity of PGF has remained elusive and ultimately limited its material performance. Here, we report the discovery of the unusual dynamic character of the C=N bonds in the aromatic pyrazine ring system under basic aqueous conditions, which enables the successful synthesis of a crystalline porous nitrogenous graphitic framework with remarkable in-plane order, as evidenced by powder X-ray diffraction studies and direct visualization using high-resolution transmission electron microscopy. The crystalline framework displays superior performance as a cathode material for lithium-ion batteries, outperforming the amorphous counterparts in terms of capacity and cycle stability.

## INTRODUCTION

The discovery of graphene as a two-dimensional (2D) sheet of fully conjugated carbons has led to a surge of research interest in diversifying its structure and properties.<sup>1–4</sup> One appealing approach is to introduce heteroatoms and nanometer-sized pores into the periodic 2D graphene layers that further stack into porous graphitic frameworks (PGFs). Such in-plane structural modification can effectively tune the band structure, introduce catalytic sites, and create guest transporting channels in three-dimensionally stacked layers,<sup>5–7</sup> which opens up a wide range of applications, including nanoelectronics, catalysis, separation, and energy storage.<sup>8–10</sup> As a representative PGF structure, PGF-1 (Figure 1) features a fully fused, nitrogen-rich aromatic 2D framework with periodic pores connected via hexaazatrinaphthalene (HATN) nodes. On account of the high lithiation capacity of HATN,<sup>11,12</sup> such a periodic framework with high-density HATN units arranged in well-defined nanochannels is especially promising for applications in lithium-ion batteries (LIBs). However, to date, the ideal PGF-1 that exhibits a high level of structural precision has not been realized as prior synthetic attempts only resulted in amorphous crosslinked microporous polymers.<sup>13–16</sup>

The great challenge of synthesizing crystalline PGF-1 lies in the lack of effective chemical tools to covalently assemble annulated aromatic units into periodic 2D

## The Bigger Picture

Insertion of well-defined, evenly spaced nanoscale pores into the two-dimensional (2D) layers of graphene invokes exciting properties due to the modulation of its electronic band gaps and surface functionalities. A bottom-up synthesis approach to such porous graphitic frameworks (PGFs) is appealing but also remains a great challenge. The current methods of building covalent organic frameworks rely on a small collection of thermodynamically reversible reactions. Such reactions are, however, inadequate in generating a fully annulated aromatic skeleton in PGFs. With the discovery of dynamic pyrazine formation, we succeeded in applying this linking chemistry to obtain a crystalline PGF material, which has displayed high electrical conductivity and remarkable performance as a cathode material for lithium-ion batteries. We envision that the demonstrated success will open the door to a wide array of fully annulated 2D porous frameworks, which hold immense potential for clean energy applications.



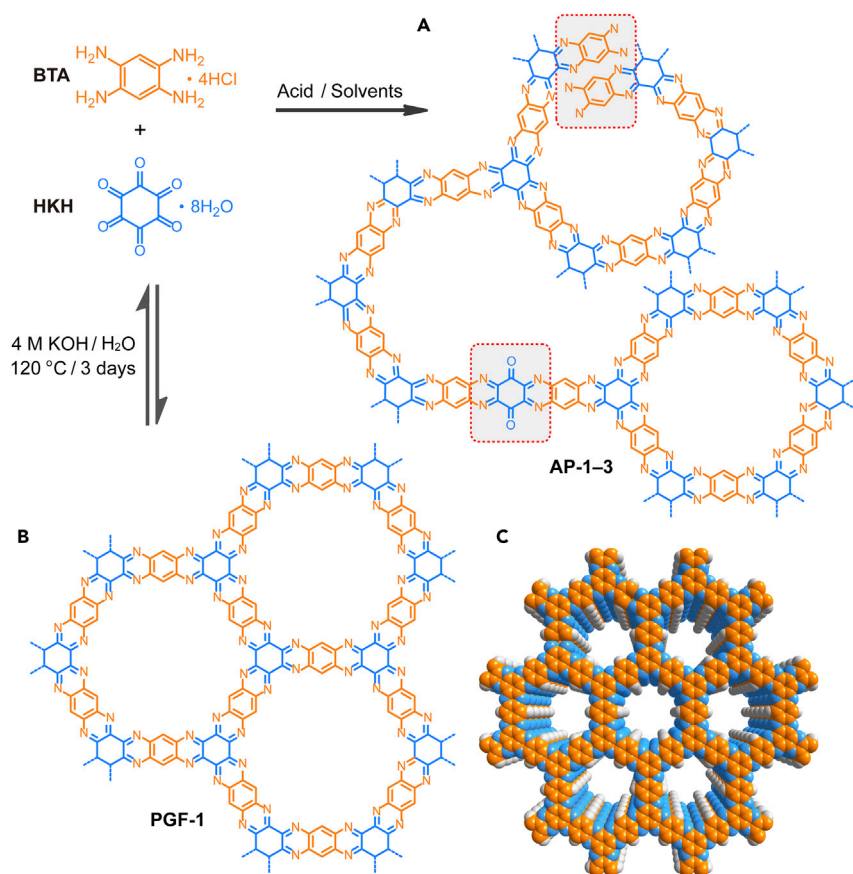


**Figure 1. Schematics of Crystalline PGF-1 and Amorphous Polymers AP-1-3**

(A) Condensation between BTA and HKH under acidic conditions leads to the formation of amorphous polymers AP-1-3 with ill-defined structures. The red boxes highlight two mishaps of connectivity that cause the loss of in-plane order. (B) Rendering the system reversible under a basic hydrothermal condition allows the formation of PGF-1 with high in-plane order. (C) Space-filling model of PGF-1 with layers arranged in an eclipsed stacking mode. Color code: C, orange; N, blue; H, gray.

sheets. Retrosynthetically, the formation of PGF-1 can be conceived by stitching the two monomeric units: C<sub>2</sub>-symmetric 1,2,4,5-benzenetetramine (BTA) tetrahydrochloride and C<sub>3</sub>-symmetric hexaketocyclohexane (HKH) octahydrate (Figure 1). Annulation occurs through the formation of the aromatic pyrazine bridging units from the condensation reaction between vicinal diamines and vicinal diketones.<sup>17</sup> The problem with this route is that the nonspecific reactive sites in BTA and HKH can lead to mishaps of connectivity, such as the example illustrated in Figure 1A. Irreversible formation of such defects will prevent the propagation of shape-persistent macrocyclic pores within the 2D plane and result in amorphous crosslinked polymers. Indeed, pyrazine formation has been deemed as an irreversible synthetic dead end because of aromatic stabilization. With few exceptions,<sup>18–22</sup> previous implementations of similar crosslinking chemistry only resulted in amorphous microporous polymers,<sup>23,24</sup> as reflected in their featureless powder X-ray diffraction (PXRD) patterns. If the condensation reaction can be rendered reversible, it may allow error-checking and self-healing to facilitate the growth of crystalline frameworks. Such dynamic covalent reactivity is the basis for the growth of the closely related covalent organic frameworks (COFs);<sup>25–27</sup> however, the majority of the known dynamic

<sup>1</sup>The Molecular Foundry, Lawrence Berkeley National Laboratory, Berkeley, CA 94720, USA

<sup>2</sup>Materials Sciences Division, Lawrence Berkeley National Laboratory, Berkeley, CA 94720, USA

<sup>3</sup>Environmental Energy Technologies Division, Lawrence Berkeley National Laboratory, Berkeley, CA 94720, USA

<sup>4</sup>Department of Materials and Engineering, Stanford University, Stanford, CA 94305, USA

<sup>5</sup>Department of Chemical and Biomolecular Engineering, University of California–Berkeley, Berkeley, CA 94720, USA

<sup>6</sup>Department of Materials Science and Engineering, University of California–Berkeley, Berkeley, CA 94720, USA

<sup>7</sup>School of Chemistry and Environment, South China Normal University, Guangzhou 510006, China

<sup>8</sup>School of Science, China University of Geosciences (Beijing), Beijing 100083, China

<sup>9</sup>National Energy R&D Center for Biorefinery, Beijing University of Chemical Technology, Beijing 100029, China

<sup>10</sup>College of Materials Science and Engineering, Nanjing Forestry University, Nanjing 210037, China

<sup>11</sup>These authors contributed equally

<sup>12</sup>Lead Contact

\*Correspondence: jianzhang@lbl.gov (J.Z.), yliu@lbl.gov (Y.L.)

<https://doi.org/10.1016/j.chempr.2020.01.011>

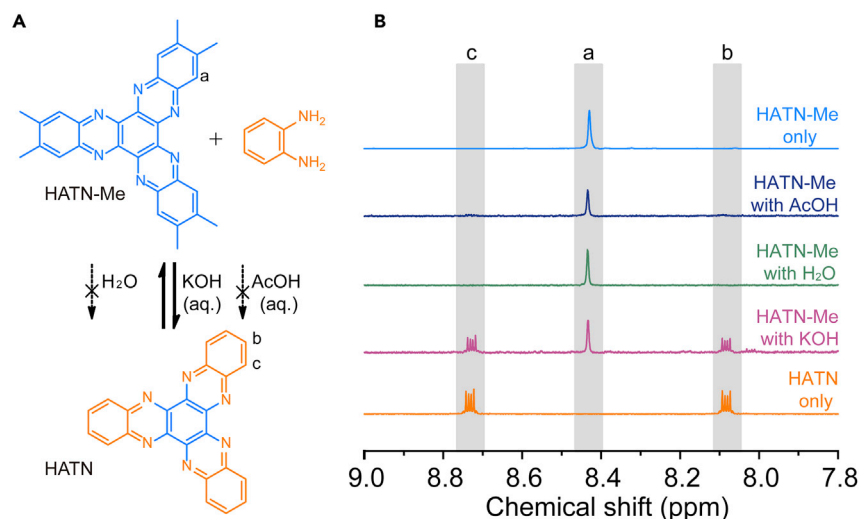


**Figure 2. Scrambling Experiments Illustrating the Dynamic Nature of Pyrazine Linkages in the HATN Ring System**

(A) Schematics of dynamic amine exchange of the pyrazine units in HATN-Me under basic hydrothermal condition. Condition: HATN-Me (1 equiv), PDA (10 equiv), KOH (6 equiv), H<sub>2</sub>O, 120°C for 3 days, N<sub>2</sub> atmosphere.

(B) Solution <sup>1</sup>H NMR spectra (500 MHz, CDCl<sub>3</sub>, 298 K) of the model compound, HATN-Me (blue), HATN (orange), and the products from reactions carried out in aqueous acetic acid (dark blue), pure water (green), and aqueous KOH (purple) at 120°C for 3 days.

covalent reactions are limited to non-annulated systems and are not applicable for the synthesis of fully annulated COFs.<sup>28</sup> Synthetic advances that can instill reversibility in annulated ring systems may thus provide a viable solution. Here, we report the discovery of reversible characteristics of the C=N bonds in the aza-fused HATN unit under simple basic aqueous conditions, which enables the successful synthesis of PGF-1 with significantly increased crystallinity compared with those in the literature and may be generalized for more annulated frameworks. We further demonstrate that when used as the cathode material in LIBs, PGF-1 significantly outperforms the non-crystalline counterparts with excellent capacity, rate capability, and cycle stability, thus highlighting their uncharted potential as high-capacity organic cathodes for LIBs.

## RESULTS

### “Scrambling” Experiments

We first conducted a series of “scrambling” experiments to validate whether amine exchange would occur in a model reaction involving hexamethyl-substituted HATN (HATN-Me) and 1,2-phenylenediamine (PDA) (Figure 2A). All the scrambling experiments, or control experiments, were conducted in aqueous conditions. At the end of the reaction, the reaction mixture was extracted by CDCl<sub>3</sub>, resulting in the complete transfer of all the solid residue into the organic phase. Given that the products of interest (HATN and HATN-Me) have poor solubility in aqueous phases, it is reasonable to assume that mass transfer is approximate to completion from the aqueous solution to the organic phase, and the observed ratio reflects the ratio of the scrambling products from the heterogeneous reaction in water. The extract was used directly for NMR spectroscopic studies unless noted otherwise (see Supplemental Information for comparisons of results from different workup procedures). No exchange product was detected when the mixture of HATN-Me and PDA at a

molar ratio of 1:10 was heated at 120°C in pure water (green curve, Figure 2B) or in an aqueous acetic acid solution (dark blue curve, Figure 2B). In sharp contrast, when the same experiment was performed in an aqueous KOH (4 M) solution, two new quartets emerged in the aromatic region of the  $^1\text{H}$  NMR spectrum at 8.73 and 8.08 ppm, characteristic of the methyl-free HATN that was formed from amine exchange with PDA. The ratio between HATN and HATN-Me based on the integration reached 45:55 after 3 days (purple curve, Figures 2B and S1). Mass spectrometry by matrix-assisted laser desorption ionization (MALDI) revealed the mass of both HATN and HATN-Me, but no detectable partially exchanged products or mono- or di-ketone intermediates (Figure S2B). Further control experiments employing only HATN-Me or PDA as the starting material did not produce HATN or decomposition product (Figures S3 and S4). Prolonged heating for 5 days or running the reaction with a larger excess (30 equiv) of PDA increased the HATN:HATN-Me ratio to 55:45 and 93:7, respectively (Figure S5). Scrambling also occurred when the reaction started with mixing HATN with 30 equiv 4,5-dimethyl-1,2-phenylenediamine, from which a HATN:HATN-Me ratio of 90:10 was observed (Figure S6). Though more details of the exchange process remain to be explored further, such experiments convincingly show that the C=N bonds in the aza-fused HATN are reversible under the base-promoted conditions.

### Structural Characterizations of PGF-1

The dynamic behavior of HATN suggested that basic conditions would similarly encourage the reversible condensation of BTA and HKH to produce frameworks with more crystalline order. With further optimization (see Table S1 for trials of different reaction conditions), crystalline PGF-1 can be reliably synthesized as a dark solid after reacting the two monomers in 4 M KOH at 120°C in a sealed reaction vessel for 3 days. Control experiments, in which individual monomer was subjected to the synthetic conditions in the absence of the other, did not yield any solid precipitate, demonstrating that PGF-1 was not from the self-polymerization of monomers. The chemical structural details of PGF-1 were characterized by various analytical techniques. The formation of pyrazine linkage was confirmed by Fourier transform infrared (FTIR) and solid-state  $^{13}\text{C}$  cross-polarization magic-angle spinning (CP-MAS at 10 KHz) NMR spectroscopies. The FTIR spectrum of PGF-1 showed the characteristic phenazine stretching bands at  $1,238\text{ cm}^{-1}$ , whereas the carbonyl vibration bands of the monomer almost disappeared (Figure S7). The solid-state  $^{13}\text{C}$  CP/MAS NMR spectrum of PGF-1 revealed only three resonances in the aromatic region (Figure 3A), in accordance with the expected symmetric structure. X-ray photoelectron spectroscopy (XPS) of PGF-1 displayed a main N1s peak at 398.6 eV (Figure S8A), close to that of HATN (398.2 eV, Figure S8B). PGF-1 is thermally stable up to 380°C before it starts to decompose under an argon atmosphere as indicated by thermogravimetric analysis (Figure S9).  $\text{N}_2$  sorption analyses performed at 77 K revealed a Brunauer-Emmett-Teller (BET) surface area of  $101\text{ m}^2\text{ g}^{-1}$  for PGF-1 (Figure S10). In addition, the Raman spectrum of PGF-1 indicated the presence of D and G bands (Figure S11), in accordance with its graphitic characteristics. An optical band gap of 1.05 eV was calculated based on its diffuse reflectance UV-vis-NIR (ultraviolet-visible-near infrared) spectrum (Figure S12), indicative of its semiconducting property. Furthermore, the environmental stability of the PGF-1 was tested by exposure in the air for 3 days or dispersing the powder in different solvents such as N-Methyl-2-Pyrrolidone (NMP), ethanol (EtOH), tetrahydrofuran (THF), toluene, acetone, methylene chloride, and acetonitrile for 24 h at room temperature. PGF-1 still retained its crystallinity, as evident from PXRD analyses (Figure S13).

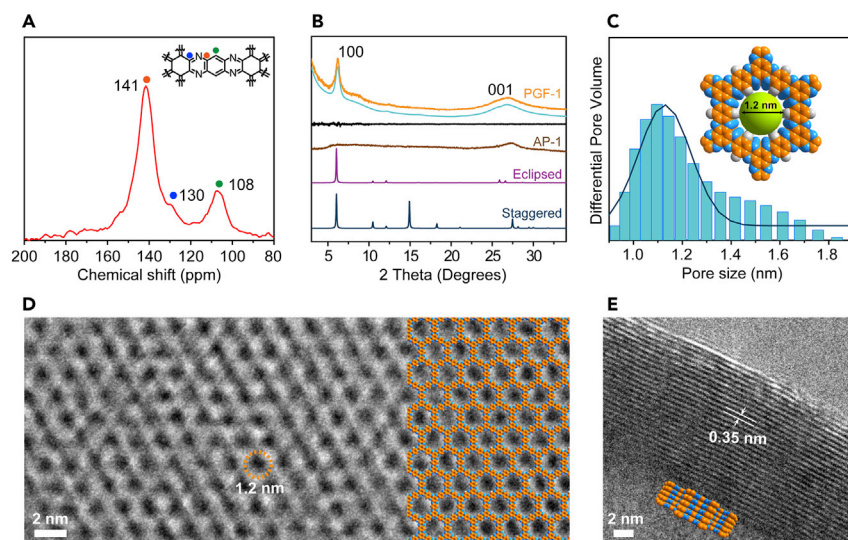


**Figure 3. Structural Characterizations of Crystalline PGF-1**

(A)  $^{13}\text{C}$  solid-state CP/MAS NMR spectra of PGF-1.

(B) PXRD profiles of PGF-1 and an amorphous analog, AP-1: experimental (orange and brown), Pawley-refined (green) and their difference spectra (black), simulated patterns using the eclipse (purple) and staggered (blue) stacking modes.

(C) Pore size distribution profile of PGF-1; inset is the predicted pore width.

(D) The Fourier-filtered HRTEM image of PGF-1 showing the ordered hexagonal pores of PGF-1. Inset is a modeled partial structure of PGF-1 overlaid on the image. Scale bar, 2 nm.

(E) The HRTEM image of PGF-1 showing the highly aligned layers of PGF-1. Scale bar, 2 nm.

### Crystallinity Studies of PGF-1

The crystallinity of PGF-1 was evaluated using PXRD and TEM analyses, in conjunction with structural simulations and Pawley refinement. The PXRD pattern of PGF-1 exhibited the most intense peak at  $6.1^\circ$ , attributable to the (100) plane spacing (Figure 3B) in the simulated structure. The peak at  $26.4^\circ$  was attributed to the (001) reflection, corresponding to a  $\pi$ - $\pi$  stacking distance of approximately 0.35 nm. Such features coincided with the simulated PXRD pattern in an AA eclipse stacking mode (purple curve in Figure 3B; also see Table S4) rather than in AB staggered stacking mode (blue curve in Figure 3B; also see Table S5). Furthermore, Pawley refinement yielded a PXRD pattern (green curve in Figure 3B), which matches well with the experimental pattern, as evident by the negligible difference (black curve) and low  $R_{\text{wp}}$  (2.94%) and  $R_p$  values (2.30%) (Table S3). The predicted pore size of 1.2 nm, based on the eclipsed stacking mode, matched well with the experimental value estimated from the adsorption isotherm by the quenched solid density functional theory model (1.12 nm, Figure 3C, inset). Good crystal habit was observed for PGF-1 by scanning electron microscopy (SEM), which displayed well-defined edges and stacked-sheet morphologies (Figure S14). Atomic force microscopy (AFM) also revealed flat regions with a thickness of 4–5 nm, corresponding to few-layer stacks of PGF-1 (Figure S15). The periodic structural features of PGF-1 were further visualized by high-resolution transmission electron microscopy (HRTEM). The highly ordered hexagonal micropores of PGF-1 were clearly visible along the [001] zone axis, with the pore diameter of  $1.2 \pm 0.1$  nm, which matched well with the simulated model (Figures 3D and S16). Moreover, lattice fringes with d-spacings of 0.84 and 0.35 nm were also observed (Figures 3E and S17), corresponding to (110) and (001) plane spacings of PGF-1, respectively. To the best of our knowledge, this represents the first example to unambiguously illustrate the in-plane pore structure



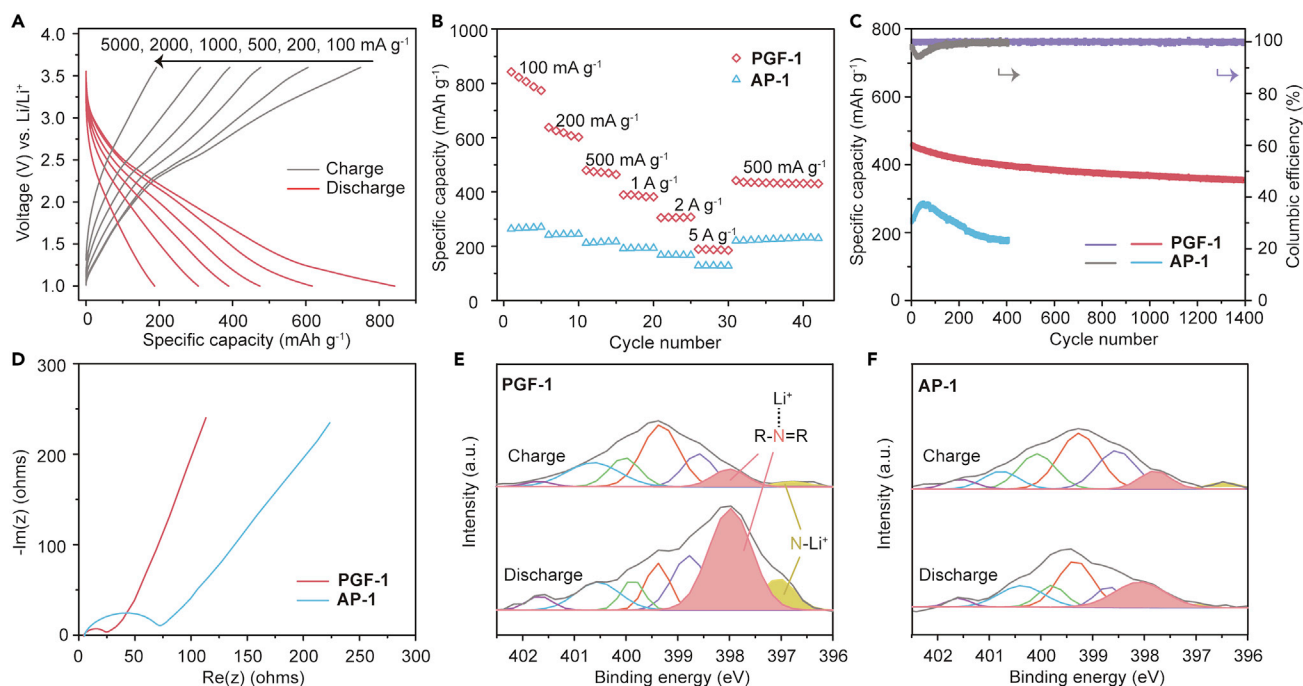


**Figure 4. Comparative Electrochemical Behavior of PGF-1 and AP-1 as Cathode Materials for LIBs**

(A) Voltage-capacity plot of PGF-1 cathode at different current densities.

(B) Rate capabilities of PGF-1 and AP-1 at various current densities.

(C) Long-term cycling performances of PGF-1 and AP-1 at a current rate of 500  $\text{mA g}^{-1}$ . Coulombic efficiency for PGF-1 (purple line) and AP-1 (gray line), specific capacity for PGF-1 (red line) and AP-1 (blue line).

(D) EIS spectra of PGF-1 and AP-1 as cathode materials in a coin cell.

(E) The XPS spectra for N1s of PGF-1 at charged and discharged states.

(F) The XPS spectra for N1s of AP-1 at charged and discharged states.

of PGF materials using TEM, which provides consistent structural details about the framework in addition to PXRD studies.

For comparison, we have separately conducted a comprehensive survey of the condensation reaction using various acidic conditions (Table S2), which produced only amorphous polymers (APs). AP-1 was the sample displaying the best in-plane crystallinity, exhibiting a broad and weak bump within the expected (100) region in its PXRD pattern (Figure 3B). Synthetic trials following literature procedures produced AP-2 and AP-3, which displayed no in-plane order (Figure S18).

### PGF-1 as Cathodes in LIBs

Inspired by the high crystallinity and HATN-containing backbone, we sought to explore the potential of PGF-1 as an alternative electrode in LIBs.<sup>29</sup> PGF-1 exhibited excellent electrochemical lithium storage capacity and rate capabilities. As illustrated in the cyclic voltammogram (Figure S19), PGF-1 displayed much higher oxidation peaks and reduction capacity within 1–3.6 V than graphene, demonstrating effective lithium storage redox processes during charging-discharging. In a half cell paired with a lithium metal anode, the PGF-1 cathode exhibited a high capacity of 842  $\text{mAh g}^{-1}$  at a current density of 100  $\text{mA g}^{-1}$ , whereas capacities of 480 and 189  $\text{mAh g}^{-1}$  were retained at high current densities of 500 and 5,000  $\text{mA g}^{-1}$ , respectively (Figures 4A and 4B). In contrast, the highest performing amorphous counterpart, AP-1, exhibited much lower capacities of 263, 212, and 128  $\text{mAh g}^{-1}$  at the current densities of 100, 500, and 5,000  $\text{mA g}^{-1}$ , respectively

(Figures 4B and S20). Under the current density of  $500 \text{ mA g}^{-1}$ , PGF-1 cathode exhibited 78.3% capacity retention after 1,400 cycles (Figure 4C), along with a high Coulombic efficiency of 99.95%, and stable charge-discharge cycles (Figure S21), whereas the lower-capacity AP-1-based cathode decayed much faster (from 236 to  $176 \text{ mAh g}^{-1}$  in only 400 cycles). The higher capacity and cycling stability observed in PGF-1 over amorphous counterparts are consistent with its improved structural regularity, which contributes favorably with more accessible active sites and the formation of continuous ion transport channels. The high cathode performance of PGF-1 was supported by a high electrical conductivity  $3 \times 10^{-3} \text{ S/m}$ , measured based on pelletized PGF-1 samples (Figure S22; Table S7), as well as the electrochemical impedance spectroscopic (EIS) studies, which revealed a significantly decreased charge transfer impedance ( $20.4 \Omega$ ) of PGF-1 than that of AP-1–3 (Figures 4D and S23). To our knowledge, the specific capacity of PGF-1 is among the highest for HATN-based materials and other organic cathode materials (Table S6).

To shed light on the crystallinity-enhanced electrochemical lithium storage behavior, we characterized the chemical composition variation during battery cycling using XPS. As illustrated in Figure 4E, PGF-1 exhibited a high-intensity, newly emerged peak at 397.9 eV in its N1s spectrum at the discharged state when compared against that of the charged state, attributable to the Li-bound pyrazine nitrogen atoms. At the same discharged state, a strong lithium-carbon peak at 284 eV in its C1s spectrum was also observed, which we attributed to Li intercalation in a 2D graphene-like layered structure and interaction with carbon species (Figure S24).<sup>30,31</sup> These data strongly suggest that both Li-N binding and Li intercalation contribute to electrochemical lithium storage in PGF-1 (Figure 4E). The low crystallinity of AP-1 results in less accessible Li-N binding sites and impedes Li intercalation, as suggested by the significantly lower Li-bound nitrogen peak at 397.9 eV in its XPS spectrum (Figure 4F), which also correlates well with its high impedance and lower LIB capacity.

## DISCUSSION

The discovery of base-promoted reversibility in HATN represents the latest addition to the limited collection of dynamic covalent reactions, with a remarkable distinction from the widely known Schiff base chemistry<sup>32</sup> and triazine chemistry,<sup>33</sup> in that it involves C=N bond breaking and reforming within an annulated aromatic ring system. Although more detailed mechanistic studies toward its dynamic nature are warranted and still underway, the unique thermodynamic feature has empowered the base-promoted hydrothermal synthesis of a porous graphitic aromatic framework, PGF-1, with remarkable in-plane crystallinity, thus opening the door to a wide array of fully annulated aromatic framework materials. When incorporated as the cathode material in LIBs, PGF-1 clearly outperforms its amorphous counterparts, underscoring the importance of minimizing structural defects and establishing long-range order for achieving higher electrochemical lithium storage capacity. Future studies on detailed ion transport mechanism in LIBs would be beneficial to further improve the material's performance as well as their use for multivalent ion batteries. Ongoing synthetic efforts are devoted to extending the chemistry to prepare PGFs with different structural features, such as the electronic structures, density of heteroatoms, and pore sizes, which will provide a broader material scope for energy storage. Such structural variation will also allude to future functional explorations of PGFs in areas beyond energy storage, such as nanoelectronics, gas separation and storage, and catalytic solar fuel conversion.



## EXPERIMENTAL PROCEDURES

### Reagents

Chemicals and solvents were obtained from commercial sources and used without further purification. Tetrahydrofuran, methanol, methylene chloride, and dimethylformamide (DMF) were purchased from Fisher Chemicals. 1,2,4,5-benzenetetramine tetrahydrochloride (purity > 95%) was purchased from AA Blocks Chemicals. Hexaketocyclohexane octahydrate (purity > 97%), potassium hydroxide, 1,2-phenylenediamine, 4,5-dimethyl-1,2-benzenediamine, scandium triflate, [Bmim]BF<sub>4</sub>, ethylene glycol, triflic acid, Triethylamine, *p*-toluenesulfonic acid monohydrate, piperidine, mesitylene, Ceric ammonium nitrate, *o*-dichlorobenzene, *n*-butanol, 1,4-dioxane, and *N*-methyl-2-pyrrolidone were purchased from Sigma-Aldrich Chemicals. Deionized water was used throughout this work.

### Instrumentation

Powder X-ray diffraction (PXRD) patterns were recorded at room temperature on a Rigaku X-ray diffractometer with Cu K $\alpha$ 1 radiation ( $\lambda$  = 1.5406 Å) at 40 kV and 40 mA. Fourier transform infrared (FTIR) spectra were recorded on a Perkin Elmer Spectrum One FT-IR system. Nitrogen sorption isotherms were obtained at 77 K with a Micromeritics Instrument Corporation model 3Flex surface characterization analyzer, and the samples were degassed under vacuum at 120°C for 12 h prior to measurement. The Brunauer-Emmett-Teller (BET) method was utilized to calculate the specific surface areas, and the pore size distribution was estimated from the adsorption isotherm by the quenched solid density functional theory (QSDFT) model. The solid-state <sup>13</sup>C CP-MAS NMR and <sup>1</sup>H NMR spectra were recorded on a Bruker Avance 500 spectrometer at a magnetic field strength of 11.7 T, corresponding to frequencies of 125.03 MHz and 500.12 MHz. The <sup>79</sup>Br MAS FID 90° pulse width was 5  $\mu$ s. The <sup>13</sup>C cross-polarization contact time was 3 ms with high power <sup>1</sup>H-decoupling. MAS experiments were performed on 4-mm MAS probes at a spinning speed of 10 kHz. The <sup>13</sup>C signals and <sup>1</sup>H signals were referenced to the methylene signal of adamantane at 38.5 ppm and 1.85 ppm, respectively. The solution <sup>1</sup>H NMR spectra was recorded on a Bruker Avance 500 II spectrometer at room temperature. Thermogravimetric analyses were carried out on a TA Instruments Q5000IR TGA under an argon flow (25 mL/min) by heating to 600°C at a rate of 10°C min<sup>-1</sup>. The solid-state UV-vis spectrum was acquired on Cary 5000 UV-Vis-NIR spectrometer. The PGF-1 sample was sonicated in *N*-Methyl-2-Pyrrolidone (NMP) for ~1 h and dropped onto a copper grid (Ultrathin C only, 300 mesh Cu). TEM images were acquired on the ThemIS microscope at 80 kV. The image aberration corrector fully corrects for coherent axial aberrations up to third order, resulting in a spatial resolution of 70 pm. In addition, imaging data were collected in high-speed Ceta2 camera (40 frames per second), at 4k  $\times$  4k resolution. X-ray photoelectron spectroscopy (XPS) measurement was performed using a Thermo Scientific K-Alpha XPS apparatus equipped with a monochromatic Al K(alpha) source and flood gun for charge compensation. SEM images were obtained with a Zeiss Gemini Ultra-55 Analytical Field Emission Scanning Electron Microscope operated at 3 kV using an in-lens detector. The atomic force microscopic (AFM) topographic images were recorded on a Dimension ICON Scanning Probe Microscope (Bruker, ICON-PKG) AFM with peak force tapping mode. The matrix-assisted laser desorption ionization (MALDI) mass spectra were acquired on a 4800 MALDI TOF/TOF analyzer from Applied Biosystems.

### Crystal Structure Modeling and Refinements

The crystal models for PGF-1 including the cell parameters and the atomic positions were simulated by Materials Studio 5.0 software package<sup>34</sup> employing the Crystal

Building module. The Pawley PXRD refinement was conducted using the Reflex module in the Materials Studio 5.0, in which a Pseudo-Voigt profile function was employed for whole profile fitting (peak broadening, peak asymmetry, and zero shift error were taken into account). The unit cell and sample parameters were refined simultaneously. The Pawley refinement results, including unit cell parameters and final related refinement factors for PGF-1 are listed in Table S3, whereas the atomic coordinates of PGF-1 crystal structure models and space-filling models are presented in Tables S4 and S5.

#### Synthesis of PGF-1

1,2,4,5-benzenetetramine tetrahydrochloride (25.6 mg, 0.09 mmol), hexaketocyclohexane octahydrate (18.6 mg, 0.06 mmol), and deionized water (2 mL) were charged in a 5-mL Microwave Biotage vial. The mixture was sonicated for 30 min to afford a slurry brown suspension. Afterward, a potassium hydroxide solution (4 M, 0.2 mL) was added, and the mixture was sonicated for another 10 min, and subsequently degassed by three cycles of freeze-pump-thaw, sealed under vacuum ( $\sim 0.12$  mBar), and heated at 120°C for 3 days. The mixture was cooled to room temperature, and the black precipitate was collected by filtration, washed with water and methanol several times, and further Soxhlet extracted with water, methanol, and methylene chloride for 3 days and dried under vacuum at 120°C for 1 day.

#### Synthesis of Amorphous AP-1

1,2,4,5-benzenetetramine tetrahydrochloride (25.6 mg, 0.09 mmol), hexaketocyclohexane octahydrate (18.6 mg, 0.06 mmol), p-toluenesulfonic acid monohydrate (0.48 mmol, 90 mg), and 2 mL of deoxygenated NMP were added in a Microwave Biotage vial (5 mL). The reaction mixture sonicated for 10 min, degassed by three cycles of freeze-pump-thaw, and heated at 120°C for 3 days. The mixture was cooled to room temperature and the resulting solid was collected by filtration; Soxhlet extracted with water, methanol, and THF for 3 days, and dried under vacuum at 120°C for 1 day.

#### Synthesis of Amorphous AP-2

The synthesis of AP-2 was based on a reported protocol with slight modifications.<sup>14</sup> 1,2,4,5-benzenetetramine tetrahydrochloride (50 mg, 0.176 mmol) and hexaketocyclohexane octahydrate (36.5 mg, 0.118 mmol) was added into a Microwave Biotage vial (5 mL) under a nitrogen atmosphere and placed in an ice bath. Deoxygenated NMP (4 mL) with 0.025 mL of sulfuric acid (>98%) was added into the vial. The reaction mixture was allowed to warm up to room temperature in 2 h. Afterward, the mixture was sealed under nitrogen and heated at 180°C for 16 h. The mixture was cooled to room temperature and the resulting solid was collected by filtration; Soxhlet extracted with water, methanol, and THF for 3 days, and dried under vacuum at 120°C for 1 day.

#### Synthesis of Amorphous AP-3

The synthesis of AP-3 was based on a reported protocol with slight modifications.<sup>15</sup> 1,2,4,5-benzenetetramine tetrahydrochloride (85.2 mg, 0.3 mmol), hexaketocyclohexane octahydrate (62.4 mg, 0.2 mmol), and a mixture of dioxane/acetic acid (1:4 v/v, 10 mL) was added into a Microwave Biotage vial (5 mL). The mixture was sonicated for 15 minutes and subsequently degassed by three cycles of freeze-pump-thaw. Afterward, the mixture was heated at 135°C for 1 week under nitrogen. The mixture was cooled to room temperature and filtered off, washing the resulting dark solid with water, HCl solution (0.2 M), methanol, and THF. The solid was Soxhlet

extracted with water, methanol, and THF for 3 days and dried under vacuum at 120°C for 1 day.

### Synthesis of Hexaazatrinaphthalene

The synthesis of hexaazatrinaphthalene (HATN) was based on a reported protocol with slight modifications.<sup>35</sup> 1,2-phenylenediamine (64.8 mg, 0.6 mmol) and hexaketocyclohexane octahydrate (33.6 mg, 0.2 mmol) were dissolved in methanol (8 mL) in a Biotage vial (20 mL). The reaction mixture was stirred at 80°C for 3 h and then stirred at room temperature overnight. After the reaction was completed, the mixture was filtrated and washed with methanol to give HATN as a yellow solid (yield: 92%). <sup>1</sup>H NMR (500 MHz, CDCl<sub>3</sub>),  $\delta$  = 8.73 (dd, 6H), 8.08 (dd, 6H). 2,3,8,9,14,15-Hexamethyl-5,6,11,12,17,18-hexaazatrinaphthalene (HATN-Me) was synthesized by analogous procedures, in which 1,2-benzenediamine was replaced by 4,5-dimethyl-1,2-benzenediamine (yield: 90%). <sup>1</sup>H NMR (500 MHz, CDCl<sub>3</sub>),  $\delta$  = 8.44 (s, 6H), 2.67 (s, 18H).

### Scrambling Experiment

HATN-Me (1.8 mg, 0.004 mmol), 1,2-phenylenediamine (4.2 mg, 0.04 mmol), potassium hydroxide aqueous solution (4 M, 0.1 mL), and 2 mL of deionized water were charged in a Microwave Biotage vial (5 mL). The reaction mixture was degassed by three cycles of freeze-pump-thaw, sealed under a nitrogen atmosphere, and stirred at 120°C for specific durations. After cooling to room temperature, the brown aqueous mixture was worked up by extracting three times with CDCl<sub>3</sub>. The CDCl<sub>3</sub> solution was subsequently used for <sup>1</sup>H NMR measurement.

### Electrochemical Testing

To prepare PGF-1 cathode, PGF-1 was dispersed in NMP, cast into three-dimension reduced graphene oxide foam current collector, and dried at 130°C using a hot plate inside an argon-filled glove box. The areal mass loading of PGF-1 was 1 mg cm<sup>-2</sup>. After drying, the prepared PGF-1 cathode was assembled into 2032-type symmetric coin cells with lithium metal as an anode, Celgard 2325 as separator, and 1 M lithium bis(trifluoromethanesulfonyl)imide in 1:1 (v/v) 1,3-dioxolane and dimethoxy ethane (DME) solution as the electrolyte. Control cathode materials followed the same electrode fabrication and battery assembling procedures. Galvanostatic cycling was conducted on an Arbin 96-channel battery tester with a voltage range of 1–3.6 V. The specific capacity was calculated based on the mass of PGF-1 active material in the cathode. The cyclic voltammetry (CV) and electrochemical impedance spectroscopy (EIS) measurements were carried out on a Biologic VMP3 system. XPS analysis was obtained on an SSI SProbe XPS spectrometer with an Al (K $\alpha$ ) source. For XPS characterizations on electrodes after cycling, the electrodes at charged and discharged state were first extracted from the coin cells disassembled in the glove box, then gently washed in DME to remove electrolyte salt residue and dried in the glove box. Before transferring into the XPS spectrometer, the XPS samples were transferred into the PHI transfer vessel in the glove box to protect it from the air.

### Electrical Conductivity Testing

To measure the conductivity of PGF-1, we pelletized PGF-1 powder using a manual press machine (Pike Technologies) into pellets with a diameter of 25 mm and a thickness of 0.3 mm. Silver paste was used to ensure good contact between the electrodes and sample. The van de Pauw method was used to measure the conductivity at room temperature.

## SUPPLEMENTAL INFORMATION

Supplemental Information can be found online at <https://doi.org/10.1016/j.chempr.2020.01.011>.

## ACKNOWLEDGMENTS

Work at the Molecular Foundry was supported by the Office of Science and Office of Basic Energy Sciences of the U.S. Department of Energy under contract no. DE-AC02-05CH11231. S.C. and B.S. are grateful for the support from the National Natural Science Foundation of China (grant no. 21603076 and 21802128, respectively). H.Z. thanks the funding support from the U.S. Department of Energy, Office of Science, Office of Basic Energy Sciences, Materials Sciences and Engineering Division under contract no. DE-AC02-05-CH11231 within the program of KC22ZH. We thank Virginia Altoe, Changlin Zhang, Chongqing Yang, Liana M. Klivansky, and Teresa Chen from the Molecular Foundry; Professor Yu Han from KAUST for their help on structural characterizations; and Professor Yi Cui from Stanford University for his support on battery characterization. We thank Stephen Whitelam and Zdenek Preisler from the Molecular Foundry for help with initial modeling. We also thank Dr. Hassan Celik, Dr. Nanette Jarenwattananon, and the SSNMR facility from the Department of Chemical and Biomolecular Engineering, University of California Berkeley for assistance with solid-state NMR measurements.

## AUTHOR CONTRIBUTIONS

Yi Liu, J.Z., E.M.C., J.C., and J.J.U. conceived the project. Yi Liu designed the experiments, X.L., H.W., and H.C. conducted the experiments and analyses. Q. Zheng, Q. Zhang, and Yawei Liu performed and with H.Z. interpreted TEM measurements. H.M. conducted and with J.A.R. interpreted solid-state NMR measurements. S.C. performed PXRD simulations and analysis. B.S. assisted with figure revisions, Raman, and AFM measurements. C.D. and M.P.G. assisted with electrical conductivity measurements. Yi Liu, E.M.C., J.C., J.J.U., X.L., H.W., and H.C. wrote and revised the manuscript. All authors discussed the results and commented on the manuscript. X.L., H.W., H.C., and Q. Zheng contributed equally to this work.

## DECLARATION OF INTERESTS

A patent application related to PGF-1 is pending.

Received: September 10, 2019

Revised: November 5, 2019

Accepted: January 16, 2020

Published: February 10, 2020

## REFERENCES

- Allen, M.J., Tung, V.C., and Kaner, R.B. (2010). Honeycomb carbon: a review of graphene. *Chem. Rev.* 110, 132–145.
- Tan, H., Tang, J., Henzie, J., Li, Y., Xu, X., Chen, T., Wang, Z., Wang, J., Ide, Y., Bando, Y., and Yamauchi, Y. (2018). Assembly of hollow carbon nanospheres on graphene nanosheets and creation of iron–nitrogen-doped porous carbon for oxygen reduction. *ACS Nano* 12, 5674–5683.
- Zakaria, M.B., Li, C., Ji, Q., Jiang, B., Tominaka, S., Ide, Y., Hill, J.P., Ariga, K., and Yamauchi, Y.J. (2016). Self-construction from 2D to 3D: one-pot layer-by-layer assembly of graphene oxide sheets held together by coordination polymers. *Angew. Chem. Int. Ed. Engl.* 55, 8426–8430.
- Salunkhe, R.R., Hsu, S.H., Wu, K.C., and Yamauchi, Y. (2014). Large-scale synthesis of reduced graphene oxides with uniformly coated polyaniline for supercapacitor applications. *ChemSusChem* 7, 1551–1556.
- Xu, B., Xiang, H., Wei, Q., Liu, J.Q., Xia, Y.D., Yin, J., and Liu, Z.G. (2015). Two-dimensional graphene-like C<sub>2</sub>N: an experimentally available porous membrane for hydrogen purification. *Phys. Chem. Chem. Phys.* 17, 15115–15118.
- Akinwande, D., Petrone, N., and Hone, J. (2014). Two-dimensional flexible nanoelectronics. *Nat. Commun.* 5, 5678.
- Jiang, D.E., Cooper, V.R., and Dai, S. (2009). Porous graphene as the ultimate membrane for gas separation. *Nano Lett.* 9, 4019–4024.
- Mahmood, J., Anjum, M.A.R., and Baek, J.B. (2018). Fused aromatic network structures as a platform for efficient electrocatalysis. *Adv. Mater.* 31, 1805062.

9. Kong, D., Gao, Y., Xiao, Z., Xu, X., Li, X., and Zhi, L.J. (2018). Rational design of carbon-rich materials for energy storage and conversion. *Adv. Mater.* **31**, 1804973.
10. Celebi, K., Buchheim, J., Wyss, R.M., Droudian, A., Gasser, P., Shorubalko, I., Kye, J.I., Lee, C., and Park, H.G. (2014). Ultimate permeation across atomically thin porous graphene. *Science* **344**, 289–292.
11. Peng, C., Ning, G.-H., Su, J., Zhong, G., Tang, W., Tian, B., Su, C., Yu, D., Zu, L., Yang, J., et al. (2017). Reversible multi-electron redox chemistry of  $\pi$ -conjugated N-containing heteroaromatic molecule-based organic cathodes. *Nat. Energy* **2**, 17074.
12. Xu, S., Wang, G., Biswal, B.P., Addicoat, M., Paasch, S., Sheng, W., et al. (2019). A nitrogen-rich 2D  $sp^2$ -carbon-linked conjugated polymer framework as a high-performance cathode for lithium-ion batteries. *Angew. Chem. Int. Ed. Engl.* **58**, 849–853.
13. Kou, Y., Xu, Y., Guo, Z., and Jiang, D. (2011). Supercapacitive energy storage and electric power supply using an Aza-fused  $\pi$ -conjugated microporous framework. *Angew. Chem. Int. Ed. Engl.* **50**, 8753–8757.
14. Wang, L., Zheng, X., Chen, L., Xiong, Y., and Xu, H. (2018). Van der Waals heterostructures comprised of ultrathin polymer nanosheets for efficient Z-scheme overall water splitting. *Angew. Chem. Int. Ed. Engl.* **57**, 3454–3458.
15. Marco, A.B., Cortizo-Lacalle, D., Perez-Miqueo, I., Valenti, G., Boni, A., Plas, J., Strutyński, K., De Feyter, S., Paolucci, F., Montes, M., et al. (2017). Twisted aromatic frameworks: readily exfoliable and solution-processable two-dimensional conjugated microporous polymers. *Angew. Chem. Int. Ed. Engl.* **129**, 7050–7055.
16. Briega-Martos, V., Ferre-Vilaplana, A., de la Peña, A., Segura, J.L., Zamora, F., Feliu, J.M., and Herrero, E. (2017). An aza-fused  $\pi$ -conjugated microporous framework catalyzes the production of hydrogen peroxide. *ACS Catal.* **7**, 1015–1024.
17. Segura, J.L., Juárez, R., Ramos, M., and Seoane, C.J. (2015). Hexaazatriphenylene (HAT) derivatives: from synthesis to molecular design, self-organization and device applications. *Chem. Soc. Rev.* **44**, 6850–6885.
18. Guo, J., Xu, Y., Jin, S., Chen, L., Kaji, T., Honsho, Y., Addicoat, M.A., Kim, J., Saeki, A., Ihee, H.J., et al. (2013). Conjugated organic framework with three-dimensionally ordered stable structure and delocalized  $\pi$  clouds. *Nat. Commun.* **4**, 2736.
19. Mahmood, J., Lee, E.K., Jung, M., Shin, D., Jeon, I.Y., Jung, S.M., Choi, H.J., Seo, J.M., Bae, S.Y., Sohn, S.D., et al. (2015). Nitrogenated holey two-dimensional structures. *Nat. Commun.* **6**, 6486.
20. Meng, Z., Aykanat, A., and Mirica, K.A. (2019). Proton conduction in 2D aza-fused covalent organic frameworks. *Chem. Mater.* **31**, 819–825.
21. Wang, M., Ballabio, M., Wang, M., Lin, H.H., Biswal, B.P., Han, X., Paasch, S., Brunner, E., Liu, P., Chen, M.J., et al. (2019). Unveiling electronic properties in metal-phthalocyanine-based pyrazine-linked conjugated two-dimensional covalent organic frameworks. *J. Am. Chem. Soc.* **141**, 16810–16816.
22. Meng, Z., Stolz, R.M., and Mirica, K.A. (2019). Two-dimensional chemiresistive covalent organic framework with high intrinsic conductivity. *J. Am. Chem. Soc.* **141**, 11929–11937.
23. Xu, J., Mahmood, J., Dou, Y., Dou, S., Li, F., Dai, L., and Baek, J.B. (2017). 2D frameworks of  $C_2N$  and  $C_3N$  as new anode materials for lithium-ion batteries. *Adv. Mater.* **29**, 1702007.
24. Talapaneni, S.N., Kim, J., Je, S.H., Buyukcakir, O., Oh, J., and Coskun, A. (2017). Bottom-up synthesis of fully  $sp^2$  hybridized three-dimensional microporous graphitic frameworks as metal-free catalysts. *J. Mater. Chem. A* **5**, 12080–12085.
25. Diercks, C.S., and Yaghi, O.M. (2017). The atom, the molecule, and the covalent organic framework. *Science* **355**, eaal1585.
26. Chen, R., Shi, J.L., Ma, Y., Lin, G., Lang, X., and Wang, C. (2019). Designed synthesis of a 2D porphyrin-based  $sp^2$  carbon-conjugated covalent organic framework for heterogeneous photocatalysis. *Angew. Chem. Int. Ed. Engl.* **58**, 6430–6434.
27. Xu, J., He, Y., Bi, S., Wang, M., Yang, P., Wu, D., Wang, J., and Zhang, F. (2019). An olefin-linked covalent organic framework as a flexible thin-film electrode for a high-performance micro-supercapacitor. *Angew. Chem. Int. Ed. Engl.* **58**, 12065–12069.
28. Ong, W.J., and Swager, T.M. (2018). Dynamic self-correcting nucleophilic aromatic substitution. *Nat. Chem.* **10**, 1023–1030.
29. Wu, J., Rui, X., Long, G., Chen, W., Yan, Q., and Zhang, Q. (2015). Pushing up lithium storage through nanostructured polyazaacene analogues as anode. *Angew. Chem. Int. Ed. Engl.* **54**, 7354–7358.
30. Ji, K., Han, J., Hirata, A., Fujita, T., Shen, Y., Ning, S., Liu, P., Kashani, H., Tian, Y., Ito, Y., et al. (2019). Lithium intercalation into bilayer graphene. *Nat. Commun.* **10**, 275.
31. Lin, Z.-Q., Xie, J., Zhang, B.-W., Li, J.-W., Weng, J., Song, R.-B., Huang, X., Zhang, H., Li, H., Liu, Y., et al. (2017). Solution-processed nitrogen-rich graphene-like holey conjugated polymer for efficient lithium ion storage. *Nano Energy* **41**, 117–127.
32. Rowan, S.J., Cantrill, S.J., Cousins, G.R., Sanders, J.K., and Stoddart, J.F. (2002). Dynamic covalent chemistry. *Angew. Chem. Int. Ed. Engl.* **41**, 898–952.
33. Kuhn, P., Antonietti, M., and Thomas, A.T. (2008). Porous, covalent triazine-based frameworks prepared by ionothermal synthesis. *Angew. Chem. Int. Ed. Engl.* **47**, 3450–3453.
34. Accelrys Software Inc. (2009, now BIOVIA). Materials Studio 5.0: Modeling Simulation for Chemical and Material, San Diego, CA.
35. Yuan, F., Li, J., Namuangruk, S., Kungwan, N., Guo, J., and Wang, C. (2017). Microporous, self-segregated, graphenel polymer nanosheets prepared by dehydrogenative condensation of aza-PAHs building blocks in the solid state. *Chem. Mater.* **29**, 3971–3979.